Sensitivity of an Electromagnetic Vector Sensor

Ekaterina Kononov[1,3], Mary Knapp[2], Alexander Morris[3], Frank Lind[2], Frank Robey[3], and Kerri Cahoy[1]

[1]Massachusetts Institute of Technology
Department of Aeronautics and Astronautics
77 Massachusetts Avenue, 33-207
Cambridge, MA 02139
kkon@mit.edu
kcahoy@mit.edu

[2]Massachusetts Institute of Technology
Haystack Observatory
99 Millstone Rd
Westford, MA 01886
mknapp@mit.edu
flind@mit.edu

[3]Massachusetts Institute of Technology
Lincoln Laboratory
244 Wood St
Lexington, MA 02421
alexander.morris@ll.mit.edu
robey@ll.mit.edu

Abstract*—High sensitivity and angular resolution radio astronomy at sub-10 MHz frequencies is only possible with a spaceborne observatory due to Earth's ionospheric cutoff frequency. Due to mass and volume constraints, sensing low frequencies on a small spacecraft necessitates an electrically small antenna with inherently low sensitivity compared to a resonant antenna. Interferometric constellations must trade off antenna sensitivity with the number of constellation elements. More complex antennas that offer significant performance advantages can potentially lower constellation sizes and make implementation more practical. The electromagnetic vector sensor antenna, composed of three dipole elements and three loop elements with a common phase center, is compact and efficient, but is new to astronomy applications and less well characterized than simpler antennas. We investigate the sensitivity of vector sensor antennas as a function of spatial direction and frequency, which are key metrics in the design and calibration of an astronomy antenna array. We start by determining the sensor's response to correlated external and uncorrelated internal noise. We then determine the sensor's system equivalent flux density (SEFD) based on optimal beamforming of the constituent loops and dipoles. We compare the SEFD with that of the more commonly-considered dipole and tripole antennas and show that a vector sensor exceeds their performance twofold. Finally, we demonstrate our method on a case study of the AERO-VISTA CubeSat mission which features a pair of deployable vector sensor antennas.

TABLE OF CONTENTS

1. INTRODUCTION

Electromagnetic vector sensors, first introduced for terrestrial applications by [1], contain three mutually orthogonal dipoles and three loop antennas, all sharing a common phase center. The vector sensor has appealing properties including the ability to beamform by direction and polarization from a single position [2] and direction finding and polarization estimation [3]. Recent work has demonstrated a vector sensor's potential for sky mapping [4], [5]. A deployable vector sensor antenna is planned for demonstration in space on the AERO-VISTA mission [6], [7] which will map Earth's auroral radio emissions from 100 kHz – 15 MHz.

There is growing interest in space-based radio astronomy at frequencies below the Earth's ionospheric cut-off ($\sim$10 MHz)[8], [9], [10]. Vector sensor antennas have not been analyzed for sensitivity to astronomical signals in the same way as more commonly used dipoles, crossed dipoles, tripoles, or search coils, especially in the context of multi-antenna interferometry. We analyze vector sensor sensitivity for comparison with other low frequency antenna technologies being considered for radio astronomy space missions.

In this paper, we analyze the system equivalent flux density (SEFD) of a vector sensor via optimal beamforming, taking into account spatially correlated and uncorrelated noise. Our method, described in Section 2, allows for antennas with heterogeneous elements (i.e., elements with differing effective lengths, receiver noise levels, radiation efficiencies, etc.) by modeling the differing frequency responses of loops and dipoles. We demonstrate the method on a case study of AERO-VISTA's deployable vector sensor implementation in Section 3. We also compare vector sensor sensitivity with that of sensors with fewer receptors. Section 4 summarizes results and provides directions for future work.

2. METHODS

Measurement Model

The vector sensor's instantaneous measurement, $\mathbf{v}_{\text{tot}}$, is the sum of contributions from the target signal $\mathbf{v}_{\text{sig}}$, external noise $\mathbf{v}_{\text{ext}}$, and internal noise $\mathbf{v}_{\text{int}}$, all of which are frequency-dependent:

$$\mathbf{v}_{\text{tot}} = \mathbf{v}_{\text{sig}} + \mathbf{v}_{\text{ext}} + \mathbf{v}_{\text{int}} \tag{1}$$

We assume that the incident signal, external noise, and internal noise are mutually uncorrelated zero-mean complex Gaussian processes. We derive the root-mean-square (RMS) voltage spectral density, in units of $\text{V}/\sqrt{\text{Hz}}$, measured at each antenna component (i.e., the standard deviation of each Gaussian). We start with the incident signal.

A completely polarized electromagnetic signal is incident from the direction (θ, ϕ). Its electric field, $\mathbf{e}$, has root-mean-square (RMS) strength E_{rms}, and polarization parameterized

This material is based upon work supported by the United States Air Force under Air Force Contract No. FA8721-05-C-0002 and/or FA8702-15-D-0001. Any opinions, findings and conclusions or recommendations expressed in this material are those of the author and do not necessarily reflect the views of the United States Air Force.

by auxiliary angle α and phase delay δ:

$$\mathbf{e} = E_{\text{rms}} \begin{bmatrix} e^{j\delta} \sin\alpha \\ \cos\alpha \end{bmatrix} \tag{2}$$

This incident field induces a voltage onto each element of the vector sensor, resulting in a measurement vector:

$$\mathbf{v}_{\text{sig}} = E_{\text{rms}} \mathbf{a}(\theta, \phi, \alpha, \delta) \tag{3}$$

where $\mathbf{a}(\theta, \phi, \alpha, \delta)$ is the array manifold. The vector sensor array manifold is given in several prior works (e.g., [1], [3], [11]), but all have subtle differences depending on choice of coordinate system, polarization parameterization, and receiving or transmitting antenna. To eliminate possible confusion, we provide the derivation used for this work in Appendix 4. Finally, the signal covariance matrix is defined as

$$\mathbf{R}_{\text{sig}} = \mathbf{v}_{\text{sig}}^H \mathbf{v}_{\text{sig}} = E_{\text{rms}}^2 \mathbf{a}\mathbf{a}^H, \tag{4}$$

where the $()^H$ superscript denotes the conjugate transpose, or Hermitian, of the vector.

Correlated External Noise

While the targeted astronomical source constitutes the signal in our application, there are many other sources, astronomical and terrestrial, radiating concurrently that may also be received by a vector sensor's full-sky field of view. We categorize these sources as interference or external noise, and process them with the array manifold in the same manner as the signal of interest because they are spatially coherent.

Sky Models—The spatially resolved sky brightness temperature (or surface brightness map) at frequencies below 30 MHz is not well characterized due to ionospheric opacity and lack of high angular resolution space-based data. There are, however, analytical and numerical projections based on observational data from higher frequencies.

To study direction-dependent effects, we use a set of sky maps generated by the Ultra Long wavelength Sky model with Absorption (ULSA) software [12]. ULSA starts with observational data at higher frequencies and adds the effect of absorption in the interstellar medium to extrapolate all-sky maps at frequencies 10 MHz and below. An example of a map generated from the ULSA model at 1 MHz is given in Figure 1. A prominent feature in this map is the dark region along the galactic equator. At higher frequencies, the emission from the interstellar medium in the plane of our galaxy makes that region bright, but in the low frequency case this model shows a cooler galactic plane/center due to free-free absorption which becomes more prominent below ∼2 MHz [13]. The low temperature region near 270° longitude is due to missing observational data, and there are several hot spots corresponding to bright sources (e.g., Cygnus A). The emissions in this map are thought to be predominantly unpolarized.

We use the ULSA model maps to study direction-dependent effects at selected frequencies (1, 3, and 10 MHz). However, generating ULSA maps for a swept frequency range would be computationally expensive. Therefore, to study trends in frequency, we instead use an isotropic unpolarized sky with mean temperature given by a scaling law [13]:

$$T_{\text{sky}} = \begin{cases} 16.3 \times 10^6 \text{ K } (\frac{\nu}{2 \text{ MHz}})^{-2.53} & \text{if } \nu > 2 \text{ MHz} \\ 16.3 \times 10^6 \text{ K } (\frac{\nu}{2 \text{ MHz}})^{-0.3} & \text{if } \nu \leq 2 \text{ MHz} \end{cases} \tag{5}$$

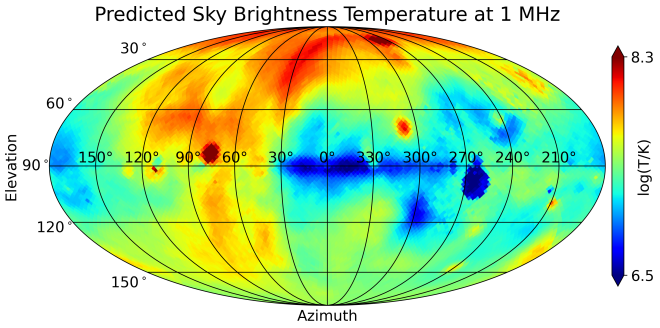

Figure 1. Example of sky temperature distribution (in galactic coordinates) created using the Ultralong-wavelength Sky Model with Absorption (ULSA) software package [12].

This model is a piece-wise power law fit for observations of the Radio Astronomy Explorer 2 (RAE-2) space mission ([14], [15]). We note that the mean sky temperatures generated at selected frequencies by the ULSA model are in agreement with the temperatures produced by this scaling law.

External Noise Covariance—The flux density contribution from a solid angle $\Delta\Omega$ in direction (θ, ϕ) is obtained from Rayleigh-Jeans law, where k_B is Boltzmann's constant and λ is wavelength:

$$S(\theta, \phi) = \frac{2k_B}{\lambda^2} T_{\text{sky}}(\theta, \phi) \Delta\Omega \tag{6}$$

Assuming that the sky background is unpolarized, the orthogonally polarized components of the incident electric field are modeled as a zero mean Gaussian with variance in terms of the flux density [16]:

$$E_\theta(\theta, \phi) \sim \mathcal{N}\left(0, \frac{\eta_0}{2} S(\theta, \phi)\right) \tag{7}$$

$$E_\phi(\theta, \phi) \sim \mathcal{N}\left(0, \frac{\eta_0}{2} S(\theta, \phi)\right) \tag{8}$$

where η_0 is the impedance of free space. To find the covariance of the signals measured by the six channels of the vector sensor, the electric field variance in each polarization is processed with the array manifold and superimposed over all directions of incidence as follows:

$$\mathbf{R}_{\text{ext}} = \sum_{\Omega} E_{\theta,\text{rms}}^2(\theta, \phi) \mathbf{a}_\theta \mathbf{a}_\theta^H + E_{\phi,\text{rms}}^2(\theta, \phi) \mathbf{a}_\phi \mathbf{a}_\phi^H \tag{9}$$

$$= \sum_{\Omega} \frac{\eta_0}{2} S(\theta, \phi)(\mathbf{a}_\theta \mathbf{a}_\theta^H + \mathbf{a}_\phi \mathbf{a}_\phi^H) \tag{10}$$

$$= \frac{k_B \eta_0}{\lambda^2} \sum_{\Omega} T_{\text{sky}}(\theta, \phi)(\mathbf{a}_\theta \mathbf{a}_\theta^H + \mathbf{a}_\phi \mathbf{a}_\phi^H) \Delta\Omega, \tag{11}$$

where $\mathbf{a}_\theta(\theta, \phi)$ and $\mathbf{a}_\phi(\theta, \phi)$ are the steering vectors for θ-polarization and ϕ- polarization respectively.

Uncorrelated Internal or Thermal Noise

Typically, the spectral noise (W/Hz) contribution from an antenna is modeled as [17]

$$P_n = k_B \tau [\eta_r T_E + (1 - \eta_r) T_p] \tag{12}$$

where τ is the mismatch loss factor, η_r is radiation efficiency, T_E is the effective antenna temperature and T_p is the physical

antenna temperature. We deviate from this model for two reasons. First, the effective antenna temperature, which is the background sky temperature weighted by the antenna radiation pattern [18], treats the external noise as spatially uncorrelated, but we treat the external noise as correlated, as described in Section 2. Second, the mismatch factor is highly dependent on receiver design and there is a tradeoff between good match and wide bandwidth. Receiver design is outside the scope of this paper and we refer the interested reader to [19]. Mismatch affects both the signal and noise generated prior to the receiver equally, and does not show in the signal to noise ratio, so we do not model it. However, noise generated within the receiver is not scaled by the mismatch loss, and can be modeled as an input-referred receiver noise temperature, T_{rx}. Finally, radiation efficiency in electrically small antennas is so low that we simplify $1 - \eta_r \approx 1$. Thus, we model the uncorrelated internal noise as the sum of the contribution from the antenna's thermal noise due to ohmic resistance, and the input-referred receiver noise temperature:

$$P_n = k_B[T_p + T_{\text{rx}}] \tag{13}$$

Since internal noise is uncorrelated, its covariance matrix $\mathbf{R}_{\text{int}}$ is a diagonal matrix with the noise power on the diagonal. The value of T_p can vary broadly depending on the spacecraft's exposure to sunlight throughout the orbit and presence of a heater or cryo-cooler to maintain the temperature. In this work, we assume $T_p = 250$ K as an average temperature in low Earth orbit. However, the exact value of T_p isn't critical for electrically small antennas because it is likely to be negligible compared with the receiver noise temperature, T_{rx}, which includes the receiver electronics noise and effects due to mismatch. In Section 3 we discuss an example where this is the case.

Beamformer Weights

The vector sensor produces a measurement for each of its constituent elements, and we seek to combine these measurements to obtain a total sensitivity metric. One way to do this is via beamforming, i.e., taking a weighted sum of the measurements. There are several options for determining beamformer weights. We use the minimum variance distortionless response (MVDR) beamformer in the following analysis because it provides the optimal weights for maximizing the signal to noise ratio (SNR) for the direction and polarization of interest [2], [20]:

$$\mathbf{w}_{\text{opt}} = \frac{\mathbf{R^{-1}a}_\psi}{\mathbf{a}_\psi^{\mathbf{H}}\mathbf{R^{-1}a}_\psi}, \tag{14}$$

where the covariance matrix $\mathbf{R} = \mathbf{R}_{\text{ext}} + \mathbf{R}_{\text{int}}$ since the external noise is uncorrelated with the internal noise. In a radio astronomy application, this matrix would apply for two cases: 1) imaging and mapping, where the correlated external noise is the signal of interest, and 2) transient detection, where it is possible to measure the noise without the signal present.

SEFD

We quantify the vector sensor's sensitivity using SEFD, a common metric in radio astronomy. SEFD is defined as the "flux density of a radio source that doubles the system temperature." [2] In other words, it is the flux density of a signal such that the SNR would be 1:1 given the level of noise in the system. It quantifies the total system noise in terms of the dimmest source that can be reliably detected (per fixed bandwidth and integration time). Thus, lower values of SEFD correspond to higher sensitivity.

An unpolarized signal incident from direction (θ, ϕ), processed with beamformer weights $\mathbf{w}$, produces beamformed output power [16]

$$P_{\text{s,out}} = \frac{\eta_0}{2} S(\theta,\phi)\, \mathbf{w^H}(\mathbf{a}_\theta\mathbf{a}_\theta^{\mathbf{H}} + \mathbf{a}_\phi\mathbf{a}_\phi^{\mathbf{H}})\mathbf{w}, \tag{15}$$

while a fully polarized signal parameterized by $\psi = (\theta, \phi, \alpha, \delta)$ yields beamformed output power

$$P_{\text{s,out}} = \eta_0 S(\theta,\phi)\, \mathbf{w^H}(\mathbf{a}_\psi\mathbf{a}_\psi^{\mathbf{H}})\mathbf{w}. \tag{16}$$

Meanwhile, the noise power at the beamformer output is [16]

$$P_{\text{n,out}} = \mathbf{w^H R w}. \tag{17}$$

SEFD is found by equating Equations (15) and (17) and solving for the flux density S, assuming that the signal of interest is unpolarized:

$$\text{SEFD}(\theta,\phi) = \frac{2}{\eta_0}\frac{\mathbf{w^H R w}}{\mathbf{w^H}(\mathbf{a}_\theta\mathbf{a}_\theta^{\mathbf{H}} + \mathbf{a}_\phi\mathbf{a}_\phi^{\mathbf{H}})\mathbf{w}} \tag{18}$$

If the signal of interest is instead assumed fully polarized, then Equation (16) is used, and the SEFD is

$$\text{SEFD}(\theta,\phi) = \frac{\mathbf{w^H R w}}{\eta_0\mathbf{w^H}(\mathbf{a}_\psi\mathbf{a}_\psi^{\mathbf{H}})\mathbf{w}}. \tag{19}$$

It may be unusual to see SEFD as a function of direction (θ, ϕ), since traditionally in radio astronomy it is given as a function of antenna noise temperature and effective area (namely, SEFD $= 2k_B T_{\text{sys}}/A_{\text{eff}}$) [21]. However, the traditional expression is applicable to antennas with narrow fields of view, and it has been shown that wide-field antennas are better characterized by a direction-dependent SEFD [22].

The next section demonstrates the application SEFD to analyze the sensitivity of AERO-VISTA's implementation of a vector sensor.

3. ANALYSIS

We validate the presented models by comparing theoretical performance of the AERO-VISTA vector sensor implementation with antenna simulations performed using Altair Feko[3], and with circuit simulations performed using the ADS software suite[4]. The results of these simulations were reported in [19]. Theoretical performance is calculated according to analytical formulas for small loop and small dipole antennas [18]. The vector sensor dimensions used for the calculations are listed in Table 1 and illustrated in Figure 2. Dipoles along the x- and y- axes are not explicitly visible in the diagram because each of the two rectangular loops has a dual feed, allowing it to serve as a dipole in differential mode and as a loop in common mode [23], [19]. Of the six antenna elements, four are unique because the x-dipole and y-dipole

[2] https://science.nrao.edu/facilities/vla/docs/manuals/oss/performance/sensitivity

[3] https://altair.com/feko

[4] https://www.keysight.com/us/en/products/software/pathwave-design-software/pathwave-advanced-design-system.html

Table 1. AERO-VISTA Antenna Dimensions[19]

Dipole length	4 m
Monopole length	2 m
X-Loop height	0.3 m
X-Loop perimeter	8.6 m
X-Loop area	1.2 m^2
P-Loop perimeter	11.3 m
P-Loop area	8 m^2
Wire diameter	0.81 mm
Wire conductivity	5.7×10^7 S/m

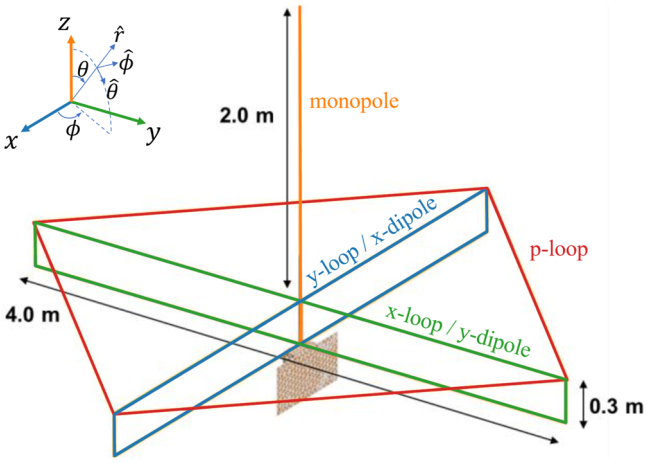

Figure 2. AERO-VISTA antenna dimensions. Modified from [19]

are identically constructed but with a 90° rotation between them about the z-axis, and the x-loop and y-loop are also identically constructed with the same 90° rotation about the z-axis. The z-dipole is realized as monopole because the spacecraft body occupies the space below the xy-plane. The z-loop is formed by a cable spanning the perimeter of the deployed x- and y-loops, and hence we refer to it as the perimeter-loop or p-loop for short.

Comparing Antenna Parameters

Figure 3 compares the radiation resistances predicted by analytical formulas (solid lines) with ones determined by electromagnetic simulation (dashed lines). The dipole and monopole analytical formulas predict a higher radiation resistance than obtained by the simulation. This is explained by effects of shadowing by the loop wires, limited counterpoise of the monopole, and losses in the mode-forming circuitry, described in [19], which are not included in the analytical model. The P-Loop shows some divergence from the simulation above 10 MHz because it is the largest loop and at high frequencies it cannot be considered electrically small, so the model breaks down. Nevertheless, the analytical results are within a factor of 2 or less of the simulation results over the majority of the frequency range of interest, indicating that the analytical model can yield relatively accurate estimates.

AERO-VISTA's design does not impedance match the receiver with the antenna, instead favoring a consistent response over a very wide bandwidth [19]. As a consequence of this design choice, the receiver sees a source impedance that

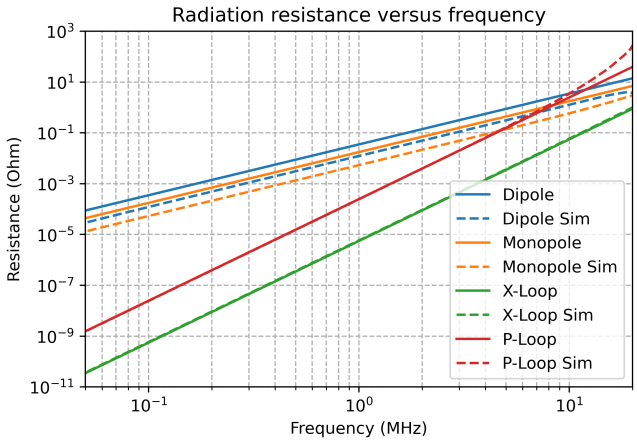

Figure 3. AERO-VISTA element radiation resistances: model versus simulation comparison.

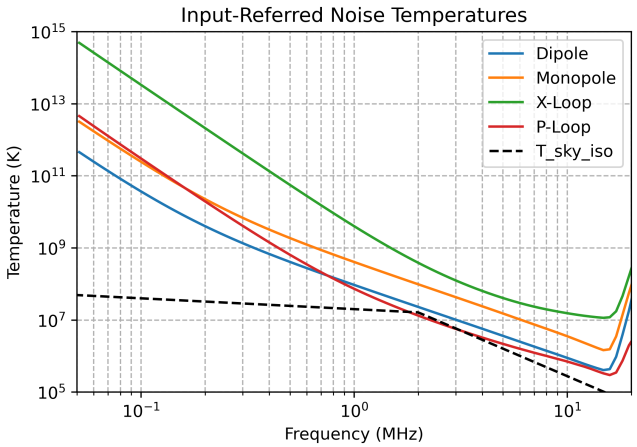

Figure 4. AERO-VISTA element input-referred noise temperatures compared with the isotropic sky temperature model from Equation (5).

deviates significantly from the optimum impedance for lowest noise figure. Receiver noise is increased and in this case it exceeds the expected external noise at most frequencies, as shown in Figure 4. The input-referred noise temperatures of Figure 4 are used to model internal noise because the thermal noise associated with the antenna's ohmic losses is negligible compared to the noise associated with the receiver's impedance mismatch.

Finally, we compare SEFD calculated via the model with that predicted by the circuit simulation on an element-by-element basis in Figure 5. The SEFD for individual elements was computed using the expression

$$\text{SEFD} = \frac{8 k_B T_{\text{sys}} R_{\text{rad}}}{\eta_0 \ell_{\text{eff}}} \tag{20}$$

where T_{sys} is the system noise temperature, R_{rad} is radiation resistance, and ℓ_{eff} is the effective length of the antenna element. Since the electromagnetic simulation assumed a fully polarized incident field, but SEFD refers to unpolarized incident field, we divide our calculated SEFD in half to consider only the co-polarized component of the incident flux. For the most sensitive elements, the dipole and P-loop, the model shows a higher flux density (lower sensitivity) than

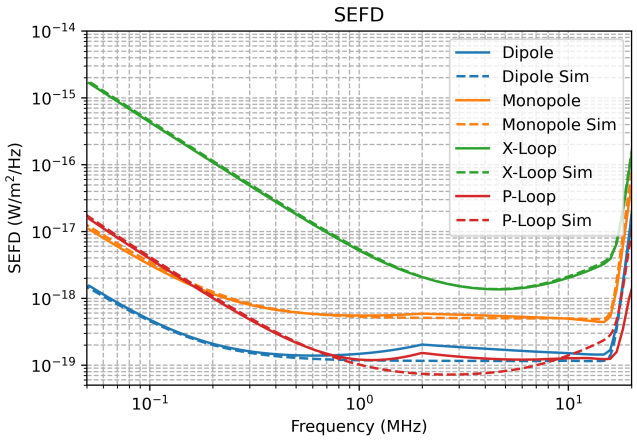

Figure 5. AERO-VISTA single-element equivalent flux densities based on our model compared with those reported by [19]. The difference is due to our model including external noise, which peaks around 2 MHz.

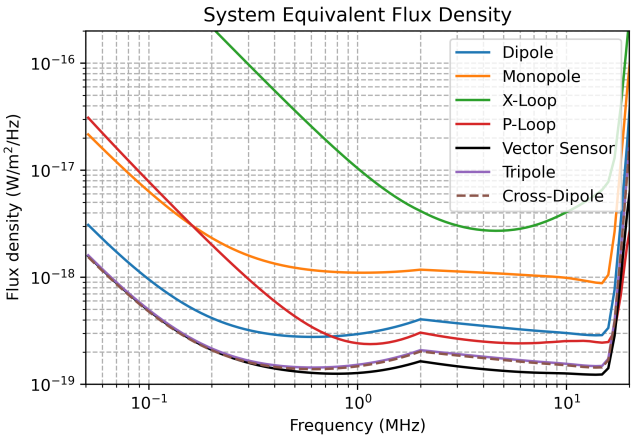

Figure 6. Comparison of AERO-VISTA's beamformed vector sensor SEFD to the SEFD of its individual elements. Also plotted are SEFD of a tripole and crossed-dipole.

the simulation around 2 MHz, despite having good agreement for frequencies above and below. This is because the external noise, which peaks in power at 2 MHz according to Equation 5, was included in the model but not in the simulation; in other words, these elements become externally noise limited in a small frequency band around 2 MHz. The monopole is barely sensitive enough to be affected by external noise, and the X-loop is unaffected.

Beamforming Performance

The SEFD of AERO-VISTA's vector sensor is computed using optimal beamforming, following the steps in Section 2. Since the vector sensor has a wide non-uniform beam-pattern, the response depends on the steering direction of the beamformer. First, we discuss a frequency sweep where we beamform in an arbitrary representative direction not aligned with any element's nulls (235° azimuth, 25° elevation), and second, we discuss a directional sweep at a fixed frequency (1 MHz). Both cases assume unpolarized incident signals.

AERO-VISTA's SEFD is plotted in Figure 6 as a function of frequency alongside the previously computed SEFD of individual elements. Figure 6 also plots the beamformed SEFD of 1) a tripole composed of just the two dipoles and monopole subset of AERO-VISTA's vector sensor, and 2) a reference crossed-dipole that is identical to AERO-VISTA's x- and y- dipoles but oriented so the direction of incidence is at its boresight. These two extra traces are plotted to illustrate the improvement in SEFD that a vector sensor has over sensors with fewer receptors, namely tripoles and crossed-dipoles.

Array gain is defined as the ratio of SNR at the beamformer output to the SNR at the input [20]. Figure 7 plots the array gain of AERO-VISTA's vector sensor and the tripole subset. Also plotted are array gains for an ideal vector sensor and an ideal tripole, which differ from AERO-VISTA by having identical elements (i.e., three identical dipoles rather than two dipoles and a shorter monopole, and x- and y-loops enlarged to be similar to the p-loop, without regard for physical implementation). The ideal vector sensor and ideal tripole elements are sized to have effective length equal to AERO-VISTA's dipoles at 1 MHz. Since AERO-VISTA's monopole is less sensitive than its dipoles, the tripole which

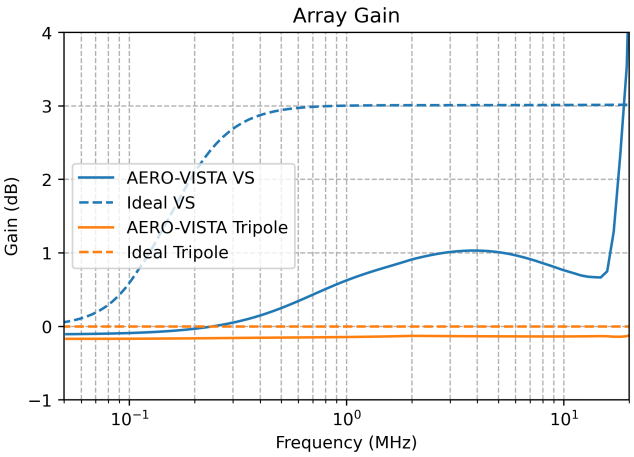

Figure 7. AERO-VISTA beamformed array gain compared with ideal antenna.

they form is slightly less sensitive than the ideal tripole. Comparing the array gain between vector sensor and tripole, we find that AERO-VISTA's loops contribute to the overall antenna sensitivity, but not as much as they could if they were bigger as in the case of the ideal vector sensor.

Finally, we examine the direction-dependent SEFD at a fixed frequency. The background sky temperature distribution, shown in Figure 1, was treated as correlated noise incident onto the vector sensor. The resulting SEFD as a function of direction is plotted in Figure 8. Two lobes are seen, one corresponding to the noisy area in the northern region of the input map, and the second a mirror image. In contrast, the same analysis of the ideal vector sensor indicated only a single lobe corresponding to the noisy area in the input map. AERO-VISTA's SEFD has two lobes due to the disparity in its elements sensitivities. The X-dipole and Y-dipole are the two most sensitive elements, so they are most impacted by external noise, but their beam patterns are symmetric in the z-direction, meaning they are incapable of distinguishing on which side of the xy-plane the direction of arrival is. The monopole and loops, dominated by internal noise, do not provide enough information to disambiguate the direction, so there is a mirror image of the noisy lobe below the xy-plane.

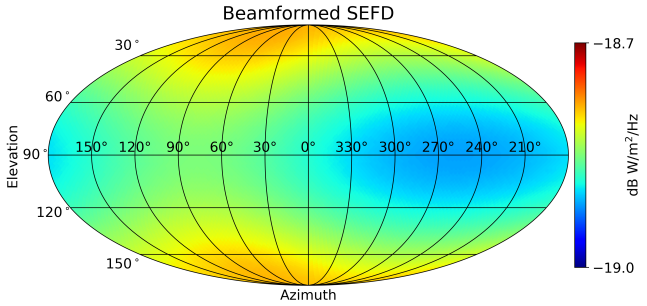

Figure 8. Direction-dependent SEFD for AERO-VISTA with correlated external noise.

Overall, this result indicates that for the given orientation of the satellite, signals measured at the galactic poles will be slightly noisier than signals measured at the galactic equator.

4. CONCLUSION

We present a generalized method for finding the direction-dependent SEFD of a vector sensor antenna. The method allows for heterogeneous antenna elements and accounts for antenna losses. We demonstrated the method on a case study of AERO-VISTA's deployable vector sensor and found the analytical results in good agreement with circuit simulations. Having a rapidly-computable analytical model is useful for designing a large astronomy array composed of this type of antenna.

We also demonstrate the sensitivity advantage of a vector sensor antenna over antennas with fewer receptors, namely tripoles and crossed-dipoles. The sensitivity advantage justifies the extra hardware mass and power consumption, which are valuable resources in space applications. This is particularly relevant for future space-based low frequency interferometric arrays, where minimizing the number of elements by maximizing the sensitivity of each element is desirable. Vector sensors may also provide valuable phase information and additional degrees of freedom to be exploited during interferometry, which is a subject of current research by the authors.

Future work could include investigating the effect of satellite attitude, particularly pointing nulls at bright interfering sources to improve performance in other directions, or mixing different attitudes of two or more satellites to fill lower sensitivity "blind spots" due to nulls in the antenna patterns. Future work can also include investigating sensitivity to polarized signals and comparing the results to those of [24]. Additionally, interaction of the plasma environment in low Earth orbit with the antenna dipole elements will effect their impedance [25] and have frequency dependent impacts on sensitivity that merit further investigation.

APPENDIX: VECTOR SENSOR ARRAY MANIFOLD

The response of an idealized vector sensor as a function of the incident signal's direction and polarization is derived by several authors, namely [1], [3], and [11], but all arrive at different formulas, which is attributed to them using different coordinate systems or receive/transmit assumptions. This work considers a receiving vector sensor in the coordinate system conventionally used in physics, illustrated in Figure 2.

We start with the polarization response, or Jones matrix, of a dipole triad, or tripole [26]:

$$\mathbf{J}_{\text{tri}} = \begin{bmatrix} \cos\theta\cos\phi & -\sin\phi \\ \cos\theta\sin\phi & \cos\phi \\ -\sin\theta & 0 \end{bmatrix} \tag{21}$$

The first three rows of the Jones matrix for a vector sensor are given by the tripole's matrix. We seek the remaining three rows which represent the loop responses to magnetic field. They are derived in [1] using a cross-product operator, based on the fact that electric field, magnetic field, and direction of propagation form an orthogonal triad.

$$\mathbf{J}_{\text{vs}} = \begin{bmatrix} \mathbf{I_3} \\ \mathbf{u}\times \end{bmatrix} \mathbf{J}_{\text{tri}} \tag{22}$$

with $\mathbf{I_3}$ as the 3×3 identity matrix, and

$$\mathbf{u}\times = \begin{bmatrix} 0 & -u_z & u_y \\ u_z & 0 & -u_x \\ -u_y & u_x & 0 \end{bmatrix} \tag{23}$$

where u_x, u_y, and u_z are the Cartesian components of the vector $\mathbf{u}$, the direction of propagation. In the present coordinate system, $\mathbf{u} = [\sin\theta\cos\phi,\ \sin\theta\sin\phi,\ \cos\theta]^{\mathbf{T}}$, which means that

$$\mathbf{u}\times = \begin{bmatrix} 0 & -\cos\theta & \sin\theta\sin\phi \\ \cos\theta & 0 & -\sin\theta\cos\phi \\ -\sin\theta\sin\phi & \sin\theta\cos\phi & 0 \end{bmatrix} \tag{24}$$

The resulting vector sensor Jones matrix is

$$\mathbf{J}_{\text{vs}} = \begin{bmatrix} \cos\theta\cos\phi & -\sin\phi \\ \cos\theta\sin\phi & \cos\phi \\ -\sin\theta & 0 \\ -\sin\phi & -\cos\theta\cos\phi \\ \cos\phi & -\cos\theta\sin\phi \\ 0 & \sin\theta \end{bmatrix} \tag{25}$$

If the incident signal's electric field polarization is described with auxiliary angle α and phase delay δ,

$$\hat{\mathbf{p}}(\alpha,\delta) = \begin{bmatrix} e^{j\delta}\sin\alpha \\ \cos\alpha \end{bmatrix}, \tag{26}$$

which is the unit vector part of Equation (2), then the idealized vector sensor's response is

$$\mathbf{v}_{\text{sig}} = \mathbf{J}(\theta,\phi)\hat{\mathbf{p}}(\alpha,\delta) \tag{27}$$

This result matches exactly the matrix given in [3] and makes clear the origin of their formulation. The matrix derived by [11], who calls it polarization response matrix, differs only in sign in the first three rows, and this is due to describing a transmitting antenna rather than a receiving one.

So far, Equation (27) represents the response of a "unit" vector sensor and it needs to be scaled by each element's effective length (effective height), the ratio between incident electric field strength (in V/m) and the open-circuit voltage induced at the antenna's terminals. Some literature refers to vector

effective length, which is the product of scalar effective length and the Jones matrix [18]. Analytical formulas approximate effective lengths of small dipoles and loops as [27]:

$$\ell_{\text{eff:dipole}} = \frac{\ell}{2} \tag{28}$$

$$\ell_{\text{eff:loop}} = jkA \tag{29}$$

where ℓ is the physical length of the dipole, A is the physical area of the loop, and $k = 2\pi/\lambda$ is the wavenumber. We construct an effective length matrix:

$$\mathbf{L}_{\text{eff}} = \begin{bmatrix} \ell/2 & 0 & 0 & 0 & 0 & 0 \\ 0 & \ell/2 & 0 & 0 & 0 & 0 \\ 0 & 0 & \ell/2 & 0 & 0 & 0 \\ 0 & 0 & 0 & jkA & 0 & 0 \\ 0 & 0 & 0 & 0 & jkA & 0 \\ 0 & 0 & 0 & 0 & 0 & jkA \end{bmatrix} \tag{30}$$

In this work, $\mathbf{L}_{\text{eff}}$ is a diagonal matrix, but its off-diagonal entries could serve to model mutual coupling between elements in future work.

Finally, the vector sensor's array manifold for a signal in the direction (θ, ϕ) with polarization (α, δ) is:

$$\mathbf{a}(\theta, \phi, \alpha, \delta) = \mathbf{L}_{\text{eff}}\mathbf{J}(\theta, \phi)\hat{\mathbf{p}}(\alpha, \delta). \tag{31}$$

ACKNOWLEDGMENTS

We would like to acknowledge the contributions of the overall AERO-VISTA team to this work. We are grateful for the support of NASA SMD Heliophysics under awards 80NSSC18K1677 and 80NSSC19K0617 which have made this work possible. Any opinions, findings, conclusions or recommendations expressed in this material are those of the author(s) and do not necessarily reflect the views of NASA. EK is grateful for the support of the MIT Lincoln Laboratory Scholars Program for funding her graduate research.

REFERENCES

[1] A. Nehorai and E. Paldi, "Vector-sensor array processing for electromagnetic source localization," *IEEE Transactions on Signal Processing*, vol. 42, no. 2, pp. 376–398, Feb. 1994.

[2] A. Nehorai, K.-C. Ho, and B. T. G. Tan, "Minimum-noise-variance beamformer with an electromagnetic vector sensor," *IEEE Transactions on Signal Processing*, vol. 47, no. 3, p. 18, 1999.

[3] K. Wong and M. Zoltowski, "Closed-form direction finding and polarization estimation with arbitrarily spaced electromagnetic vector-sensors at unknown locations," *IEEE Transactions on Antennas and Propagation*, vol. 48, no. 5, pp. 671–681, May 2000.

[4] M. Knapp, F. Robey, R. Volz, F. Lind, A. Fenn, A. Morris, M. Silver, S. Klein, and S. Seager, "Vector antenna and maximum likelihood imaging for radio astronomy," in *2016 IEEE Aerospace Conference*. Big Sky, MT, USA: IEEE, Mar. 2016, pp. 1–17.

[5] R. Volz, M. Knapp, F. D. Lind, and F. C. Robey, "Covariance estimation in terms of Stokes parameters with application to vector sensor imaging," in *2016 50th Asilomar Conference on Signals, Systems and Computers*. Pacific Grove, CA, USA: IEEE, Nov. 2016, pp. 1339–1343.

[6] P. J. Erickson, G. Crew, M. Hecht, M. Knapp, F. Lind, R. Volz, W. Ma, J. LaBelle, J. W. LaBelle, F. Robey, W. St, L. Ma, K. Cahoy, B. Malphrus, J. Vierinen, and A. Weatherwax, "AERO: Auroral Emissions Radio Observer," in *Proceedings of the AIAA/USU Conference on Small Satellites*, 2018, p. 10.

[7] F. D. Lind, P. J. Erickson, M. Hecht, M. Knapp, G. Crew, R. Volz, J. Swoboda, F. Robey, M. Silver, A. J. Fenn, W. St, L. Ma, B. Malphrus, and K. Cahoy, "AERO & VISTA: Demonstrating HF Radio Interferometry with Vector Sensors," in *Proceedings of the AIAA/USU Conference on Small Satellites*, 2019, p. 11.

[8] B. Cecconi, M. Dekkali, C. Briand, B. Segret, J. N. Girard, A. Laurens, A. Lamy, D. Valat, M. Delpech, M. Bruno, P. Gélard, M. Bucher, Q. Nenon, J.-M. Grießmeier, A.-J. Boonstra, and M. Bentum, "NOIRE study report: Towards a low frequency radio interferometer in space," in *2018 IEEE Aerospace Conference*, Mar. 2018, pp. 1–19.

[9] M. J. Bentum, M. K. Verma, R. T. Rajan, A.-J. Boonstra, C. J. M. Verhoeven, E. K. A. Gill, A. J. van der Veen, H. Falcke, M. K. Wolt, B. Monna, S. Engelen, J. Rotteveel, and L. I. Gurvits, "A Roadmap towards a Space-based Radio Telescope for Ultra-Low Frequency Radio Astronomy," *Advances in Space Research*, vol. 65, no. 2, pp. 856–867, Jan. 2020.

[10] K. Z. Adami and I. O. Farhat, "Low-frequency technology for a lunar interferometer," *Philosophical Transactions of the Royal Society A: Mathematical, Physical and Engineering Sciences*, vol. 379, no. 2188, p. 20190575, Jan. 2021.

[11] A. J. Fenn, "Vector Sensor Array Antennas," in *Electromagnetics and Antenna Technology*. Artech House, 2017, pp. 289–309.

[12] Y. Cong, B. Yue, Y. Xu, Q. Huang, S. Zuo, and X. Chen, "An Ultralong-wavelength Sky Model with Absorption Effect," *The Astrophysical Journal*, vol. 914, no. 2, p. 128, Jun. 2021.

[13] S. Jester and H. Falcke, "Science with a lunar low-frequency array: From the dark ages of the Universe to nearby exoplanets," *New Astronomy Reviews*, vol. 53, no. 1, pp. 1–26, May 2009.

[14] H. V. Cane, "Spectra of the non-thermal radio radiation from the galactic polar regions," *Monthly Notices of the Royal Astronomical Society*, vol. 189, no. 3, pp. 465–478, Dec. 1979.

[15] J. C. Novaco and L. W. Brown, "Nonthermal galactic emission below 10 megahertz," *The Astrophysical Journal*, vol. 221, p. 114, Apr. 1978.

[16] S. W. Ellingson, "Sensitivity of Antenna Arrays for Long-Wavelength Radio Astronomy," *IEEE Transactions on Antennas and Propagation*, vol. 59, no. 6, pp. 1855–1863, Jun. 2011.

[17] S. R. Best, "Optimizing the receiving properties of electrically small HF antennas," *URSI Radio Science Bulletin*, vol. 2016, no. 359, pp. 13–29, Dec. 2016.

[18] C. A. Balanis, *Antenna Theory : Analysis and Design*, fourth edition. ed. Hoboken, New Jersey: John Wiley & Sons, 2016.

[19] A. Morris, A. Fenn, M. Silver, A. Lopez, M. Knapp, F. Lind, and P. J. Erickson, "Design of a Space-Based HF Vector Sensor Antenna Array for the AERO-VISTA Mission," in *2022 IEEE International Symposium on*

Phased Array Systems & Technology (PAST), Oct. 2022, pp. 1–8.

[20] H. L. Van Trees, *Detection, Estimation, and Modulation Theory, Part 4: Optimum Array Processing*. John Wiley & Sons, Inc., 2002.

[21] J. M. Wrobel and R. C. Walker, "Sensitivity," *Astronomical Society of the Pacific Conference Series*, vol. 180, p. 171, 1999.

[22] A. T. Sutinjo, M. Sokolowski, M. Kovaleva, D. C. X. Ung, J. W. Broderick, R. B. Wayth, D. B. Davidson, and S. J. Tingay, "Sensitivity of a low-frequency polarimetric radio interferometer," *Astronomy & Astrophysics*, vol. 646, p. A143, Feb. 2021.

[23] R. King, "The rectangular loop antenna as a dipole," *IRE Transactions on Antennas and Propagation*, vol. 7, no. 1, pp. 53–61, Jan. 1959.

[24] Sutinjo, A. T., Ung, D. C. X., and Sokolowski, M., "System equivalent flux density of Stokes I, Q, U, and V of a polarimetric interferometer," *A&A*, vol. 664, p. A102, 2022.

[25] K. Balmain, "The impedance of a short dipole antenna in a magnetoplasma," *IEEE Transactions on Antennas and Propagation*, vol. 12, no. 5, pp. 605–617, 1964.

[26] A. T. Sutinjo, M. Kovaleva, and Y. Xu, "System Equivalent Flux Density of a Polarimetric Tripole Radio Interferometer," *Publications of the Astronomical Society of the Pacific*, vol. 134, no. 1031, p. 014502, Jan. 2022.

[27] F. C. Robey, M. Knapp, A. J. Fenn, M. Silver, K. Johnson, F. J. Lind, R. Volz, S. Seager, and F. Neylon-Azad, "High Frequency (HF) Radio Astronomy from a Small Satellite," in *Proceedings of the AIAA/USU Conference on Small Satellites*, 2016, p. 18.

BIOGRAPHIES

Ekaterina Kononov *received B.S. and M.Eng. degrees in Electrical Engineering in 2012 and 2013 from the Massachusetts Institute of Technology. She is currently a graduate research fellow in the Department of Aeronautics and Astronautics at MIT and an associate technical staff member at Lincoln Laboratory. Her Ph.D. work is on space systems and computational imaging with vector sensor arrays. Prior to starting the Ph.D. program, Kononov worked on wireless communication and radar technology at Lincoln Laboratory and Maxim Integrated.*

Mary Knapp *received a BS in Aerospace Engineering at MIT in 2011 and PhD in Planetary Science in 2018 and is currently a Research Scientist at MIT Haystack Observatory. Her research focus is the detection and characterization of exoplanetary magnetic fields via low frequency radio emission. She is currently a NIAC Fellow for GO-LoW, the Great Observatory for Long Wavelengths. Her additional research interests include the development of small spacecraft for astronomy and planetary science. Dr. Knapp served as project scientist for the ASTERIA CubeSat since 2010 through launch and operations until end of mission and is currently the deputy PI for the AERO-VISTA twin CubeSat mission to study Earth's auroral radio emission.*

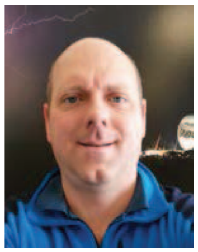

Frank Lind *studied at the University of Washington where he received a BS degree in Physics (with honors) and a BS degree in Computer Science in 1994. He then joined the UW Geophysics Program and pursued studies leading to a Ph.D. in Geophysics in 1999. His work there focused on Passive Radar Observations of the Aurora Borealis. Currently, Lind's scientific and technical research at MIT Haystack Observatory focuses on radar and radio studies of the space environment, passive radar, incoherent scatter radar, ionospheric plasma physics, software radio and radar signal processing, and distributed sensor systems. At the Observatory he leads the technical team for the NSF sponsored Millstone Hill Geospace Facility and instrument development efforts for a variety of advanced radio telescopes, array radars, and distributed sensor networks. He is the former chair of USNC URSI Commission G.*

Frank Robey *received BSEE (Summa Cum Laude) and MSEE degrees from U. Missouri-Columbia and D.Sc. EE in adaptive detection and beamforming from Washington U. He has been with MIT Lincoln Laboratory for more than 25 years. At Lincoln he has lead multiple fundamental and applied research initiatives including advanced sensor technology, coherent Multiple-Input Multiple-Output (MIMO) radar, electronic intelligence and next generation over-the-horizon radar. He spent two years on assignment as the Deputy Director of Smart Collection at IARPA/ODNI. He began his career as a precision instrument designer at Hewlett Packard and then at Emerson Electric.*

Kerri Cahoy *is an Associate Professor of Aeronautics and Astronautics at MIT and leads the Space Telecommunications, Astronomy, and Radiation (STAR) Laboratory. Cahoy received a B.S. (2000) in Electrical Engineering from Cornell University, and M.S. (2002) and Ph.D. (2008) in Electrical Engineering from Stanford University. Dr. Cahoy previously worked as a Senior RF Communications Engineer at Space Systems Loral, and as a postdoctoral fellow at NASA Ames. Cahoy currently works on nanosatellite atmospheric and ionospheric sensing missions (MicroMAS, NASA TROPICS, AERO-VISTA), optical communications (NASA CLICK), and exoplanet technology demonstration (DARPA DeMi) missions.*

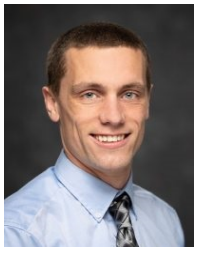

Alexander Morris *received the B.S. and M.S. degrees in electrical engineering from the University of Alaska Fairbanks, in 2011 and 2014, respectively. Since then, he has been with MIT Lincoln Laboratory in Lexington, MA, where holds the position of associate technical staff.*